Journal of Nanobiotechnology

RESEARCH

Open Access

Lanthanide-specific doping in vacancy-engineered piezocatalysts induces lysosomal destruction and tumor cell pyroptosis

Xiaoyan Li[1], Ying Wang[2], Xinyue Cao[1], Xinran Song[3], Liang Chen[4], Meiqi Chang[5*], Yu Chen[4*] and Bingcang Huang[1*]

Abstract

Background Reactive oxygen species (ROS)-mediated pyroptosis provides a robust strategy for overcoming apoptosis resistance in breast cancer therapy. Nevertheless, the low efficiency of pyroptosis remains an undeniable challenge. Overcoming this obstacle necessitates the creation of innovative approaches and nanocatalysts to boost ROS generation. Herein, the distinct lanthanum-doped $BiFeO_3$ (La-BFO) piezoelectric nanozymes are rationally designed and engineered for the specific cell pyroptosis of breast cancer through inducing the amplified production of ROS and releasing La ions.

Results The introduction of La reduces the recombination rate of electron-hole pairs through narrowing the bandgap and creating the oxygen vacancy of BFO, improving the harmful ROS generation efficiency. Importantly, the released La ions robustly disrupt the lysosomal membrane, ultimately inducing cell pyroptosis, in combination with ROS-induced biological effect.

Conclusion In vitro and in vivo antineoplastic results confirm the desirable therapeutic effect on combating tumor. Especially, the iron and bismuth elemental components endow the nanocomposites with dual-mode computed tomography/magnetic resonance imaging ability, guaranteeing the potential therapeutic guidance and monitoring.

*Correspondence:
Meiqi Chang
changmeiqi@vip.sina.com
Yu Chen
chenyuedu@shu.edu.cn
Bingcang Huang
hbc01275@glhospital.com
[1]Department of Radiology, Gongli Hospital of Shanghai Pudong New Area, Shanghai 200135, P. R. China
[2]Sino-French Cooperative Central Lab, Gongli Hospital of Shanghai Pudong New Area, Shanghai 200135, P. R. China
[3]School of Environmental and Chemical Engineering, Shanghai University, Shanghai 200444, P.R. China
[4]Materdicine Lab, School of Life Sciences, Shanghai University, Shanghai 200444, P. R. China
[5]Laboratory Center, Shanghai Municipal Hospital of Traditional Chinese Medicine, Shanghai University of Traditional Chinese Medicine, Shanghai 200071, P. R. China

Graphical Abstract

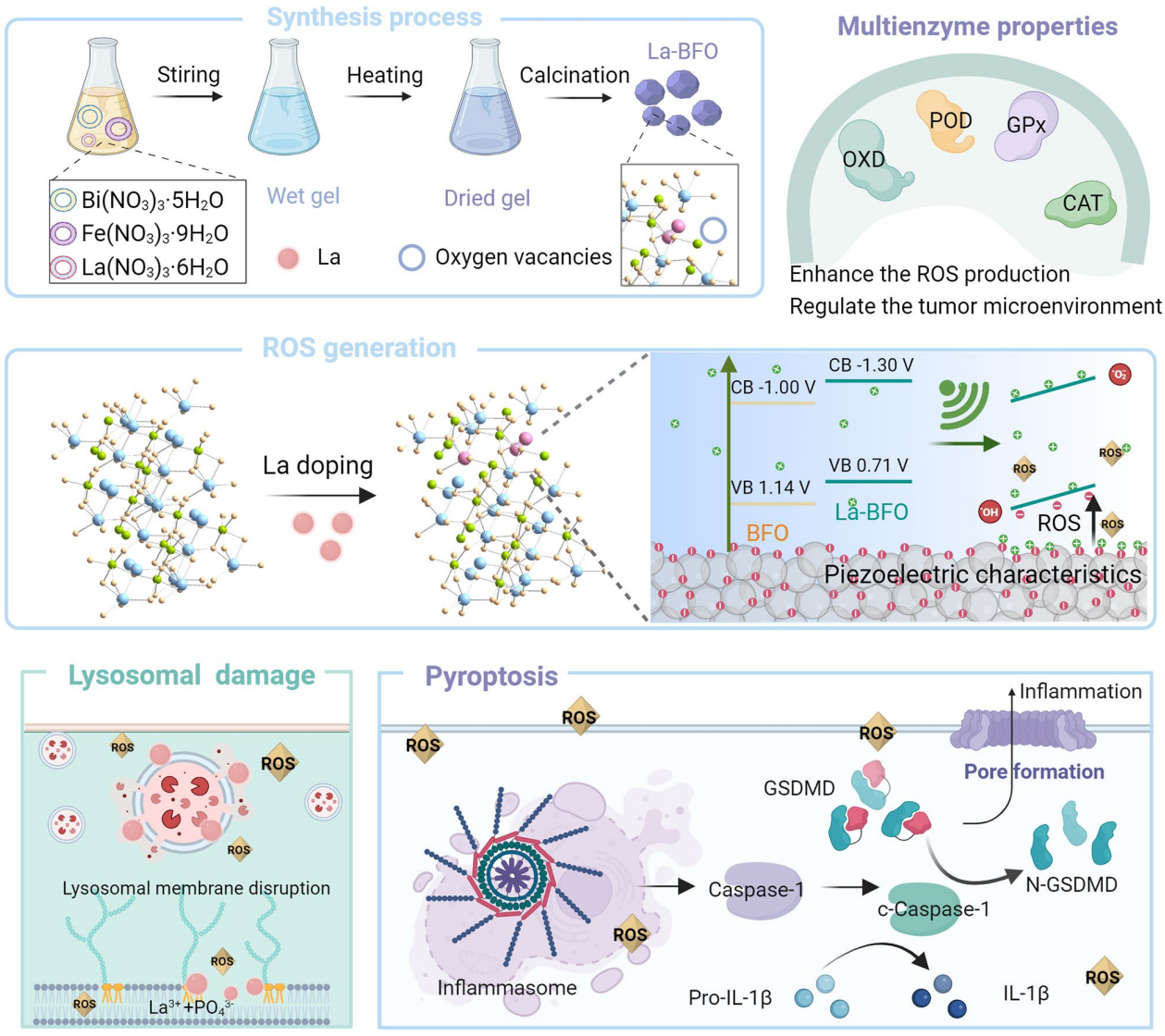

Keywords Piezoelectric therapy, Oxygen vacancy, Sonosensitizer, Nanomedicine, Pyroptosis

Introduction

Tumor resistance to apoptosis and immunosuppressive nature of the tumor microenvironment are two primary factors contributing to the poor outcomes of tumor treatment [1, 2]. Pyroptosis, emerging as a novel form of programmed cell death, has found broad application in the realm of malignant tumor treatment owing to its substantial tumor suppression [3, 4]. Pyroptosis is orchestrated by the gasdermin (GSDM) family. Specifically, certain caspases cleave the linker of GSDM, producing a GSDM-N fragment capable of perforating membranes, thereby instigating pyroptosis [5–8]. Considering that antineoplastic efficacy is seriously reduced by the resistance of cancer cells to apoptosis, the emergence of pyroptosis provides a new choice [9].

Biological and medical technologies involving reactive oxygen species (ROS) have garnered considerable attention [10, 11]. ROS generation is a classic mechanism associated with the induction of pyroptosis [12]. For instance, Kim et al. designed a compound NI-TA that catalyzes the production of superoxide anions to induce cell pyroptosis. ROS generated by NI-TA specifically activate caspase-3, leading to the cleavage of GSDME, thereby triggering the formation of membrane pores and resulting in the release of pro-inflammatory cytokines such as IL-1β and LDH leakage [13]. Our group designed

$LaFeO_3$ perovskite nanocrystals as the pyroptosis inducer for the ROS burst-induced pyroptosis process through the ROS-NLRP3-GSDMD pathway [5].

Among various tumor treatment methods involving ROS induced by external fields, piezoelectric catalytic therapy based on sonocatalysis stands out as a treatment approach with low side effects, non-invasiveness, and high tumor specificity [14, 15]. By integrating exogenous ultrasound with piezoelectric materials to trigger specific sonocatalytic reactions, substantial amounts of cytotoxic ROS are produced, thereby effectively targeting and eliminating tumor cells [16–18]. $BiFeO_3$, a typical piezoelectric material, can convert mechanical energy into electrical signals through the piezoelectric effect [19]. It enhances the migration and separation of photogenerated electrons and holes, thereby promoting redox reactions and generating active substances capable of effectively eliminating tumor cells [20]. However, the wide band gap and unsatisfactory ROS production efficiency restricted its further biological applications. The surface interface of a catalyst serves as a crucial site for molecular reactions, energy transfer, carrier separation, and migration [21]. Strategically adjusting the electronic and geometric structure of the interface through a tailored interface strategy can effectively enhance carrier separation and transport efficiency, thus improving catalytic activity. Introducing metal ions can regulate the electronic and geometric structure of catalysts, effectively altering the pathways for charge carrier transfer [22]. This is crucial for enhancing the efficiency of electron-hole separation. Among them, La ion doping has been reported to reduce the band gap and improve the efficiency of ROS production [23]. More importantly, La ions can also induce pyroptosis by destroying the lysosomal membrane [24].

In this work, we rationally designed lanthanum-doped $BiFeO_3$ (La-BFO) piezoelectric nanozymes as pyroptosis inducers for breast cancer treatment by ameliorating the tumor microenvironment, promoting the amplification of ROS and releasing La ions (Scheme 1). The incorporation of La decreases the band gap of BFO and lowers the recombination rate of electron-hole pairs, thereby enhancing the generation efficiency of deleterious ROS. Notably, the released La ions can significantly disrupt the lysosomal membrane and synergistically interact with ROS to induce pyroptosis. The results of RNA sequencing, morphological observation, and western blot analysis fully confirmed the involvement of ROS activation and the La^{3+}-induced Caspase-1/GSDMD pathway in the pyroptosis-related anti-tumor process. Additionally, the incorporation of iron and bismuth elements provides dual-modal imaging capabilities, facilitating both magnetic resonance imaging (MRI) and computed tomography (CT) with La-BFO. Overall, this study introduces a unique approach to treating breast cancer by optimizing piezoelectric nanozymes via functional ion engineering, thereby showcasing the substantial potential of merging nanobiotechnology with imaging technology for tumor diagnosis and treatment.

Results and discussion

Synthesis and characterization of La-BFO

BFO and La-BFO piezoelectric nanozymes were fabricated by a facile sol-gel method (Fig S1). Transmission electron microscopy (TEM) image and size distribution plot reveal the particle-like morphology of La-BFO with average particle sizes of 200.7 ± 2.95 nm (Fig. 1a and c). The high-resolution TEM (HRTEM) image demonstrates the crystalline characteristics of La-BFO with a lattice fringe distance of 0.27 nm, which corresponds to the (110) plane of $BiFeO_3$ (Fig. 1b) [25, 26]. Energy dispersive X-ray spectroscopy (EDS) clearly shows the presence of Bi, Fe, La, and O, and the homogeneous distributions of elements were confirmed by elemental mapping results (Fig. 1d and e). Furthermore, the crystalline structures of BFO and La-BFO were further confirmed by X-ray diffraction (XRD) measurement (Fig. 1f). For BFO, the diffraction peaks at 22.4°, 31.8°, 32.1°, 39.5°, 45.8°, 51.3°, 57.2° and 67.0° correspond to (012), (104), (110), (202), (024), (116), (214) and (220) crystal planes of $BiFeO_3$ (JCPDS No. 86-1518) with a rhombic R3c structure [27]. The overlap of the main diffraction peaks indicates that the introduction of La causes minimal lattice distortion in the structure of $BiFeO_3$.

In addition, the elemental composition and valence states of the products were determined by XPS analyses (Fig. 1g, Fig S2). In the high-resolution spectrum of La 3d, the peaks at 855.4 eV and 851.7 eV correspond to La $3d_{3/2}$, and the peaks at 838.5 eV and 834.8 eV are indexed to La $3d_{5/2}$. A spin-orbit splitting of 16.9 eV occurs between La $3d_{3/2}$ and La $3d_{5/2}$, which attests to the presence of La^{3+}. Bi $4f_{7/2}$ and Bi $4f_{5/2}$ at 159.2 and 164.5 eV have spin-heavy states that correlate with the Bi^{3+}. Peaks at 710.9 and 724.1 eV are attributed to Fe $2p_{3/2}$ and Fe $2p_{1/2}$, and the spin-orbit splitting energy of 13.2 eV confirms the valence state of Fe^{3+} [28]. O 1s spectra of BFO and La-BFO were measured to evaluate the generation of oxygen vacancies (Fig. 1h and i). For BFO, the O 1s spectrum can be deconvolved into two peaks at 530.7 eV and 529.6 eV, corresponding to surface-adsorbed oxygen and lattice oxygen, respectively. By contrast, the peaks at 531.9 eV, 530.1 eV and 528.5 eV in the La-BFO sample could be ascribed to the surface-adsorbed oxygen, oxygen vacancy and lattice oxygen. It is concluded that doping of La ions induces the generation of oxygen vacancies.

The piezoelectric effect of La-BFO resulting from ultrasonic stress can be verified through the measurement of local piezoelectric signals using piezoresponse

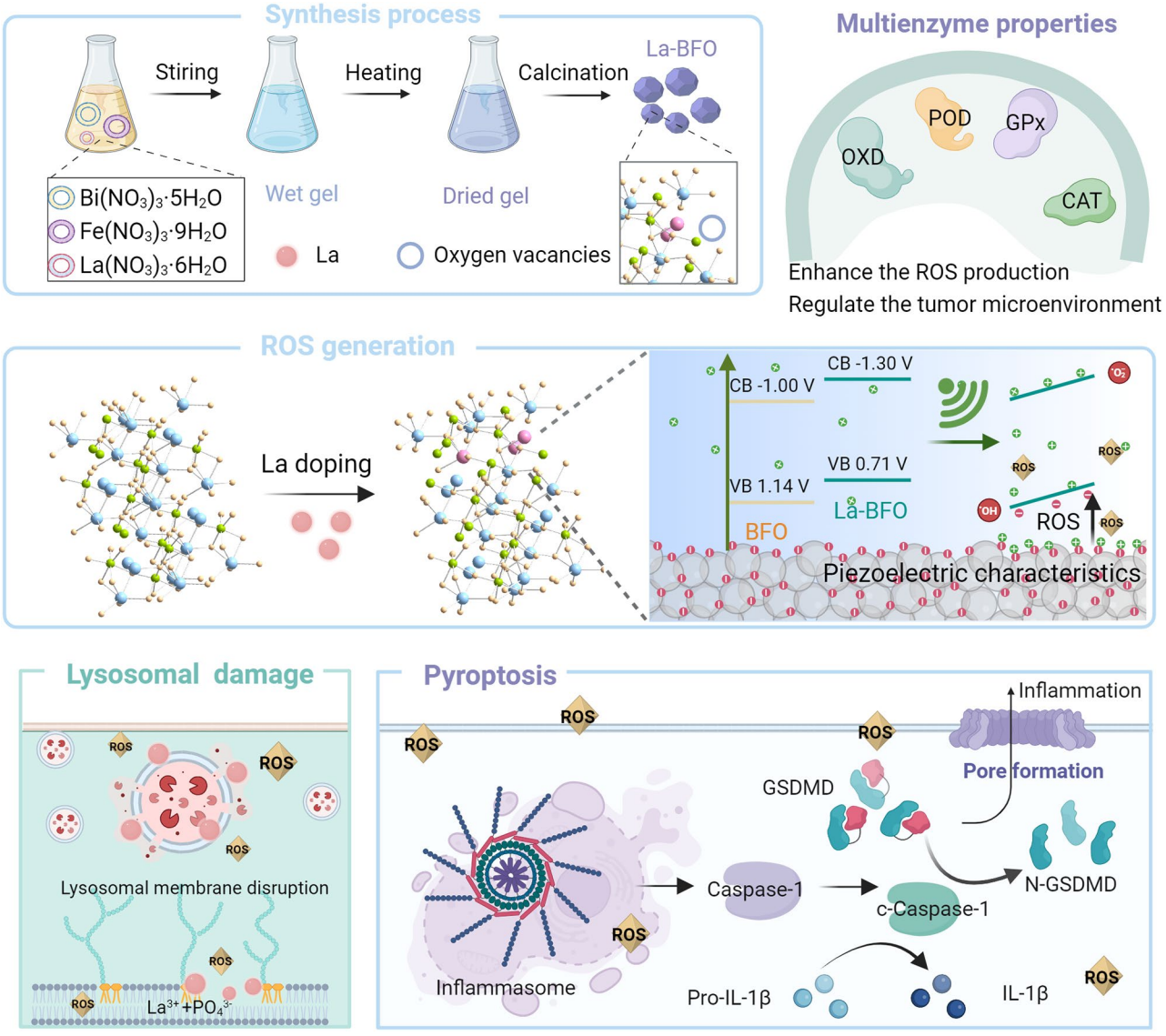

Scheme 1 Schematic illustration of bandgap change, multienzyme-mimicking activities and pyroptosis mechanism of La-BFO. La-doped BFO piezoelectric nanozyme triggers the enlarged ROS generation by lowering the band gap and forming oxygen vacancies and induces lysosomal damage through the release of La ions, ultimately inducing cancer-cell pyroptosis

force spectroscopy (PFM) [29]. The amplitude and phase images of La-BFO exhibit various color and intensity contrasts, indicating distinct orientations of piezoelectric polarization (Fig S3). Figure 1j depicts the phase voltage hysteresis return line, which exhibits a 180° variation under a 10 V DC bias field, indicating a local polarization switching phenomenon. Moreover, the appearance of an amplitude-voltage butterfly ring further validates the remarkable local piezoelectric properties of La-BFO. The UV absorption spectra of BFO and La-BFO confirmed their semiconductor characteristics (Fig. 1k). The band gap values of 2.14 eV and 2.01 eV were measured using the derivative Tauc plot, which indicated the role of La ions in reducing band gaps. In addition, the XPS valence band spectra were employed to elucidate the positions of the valence bands of BFO and La-BFO. The corresponding values are 1.14 eV and 0.71 eV, respectively (Fig. 1l). Based on these results, the explosive production of ROS is facilitated by the piezoelectric effect and La doping. The piezoelectric potential acts as an internal electric field, modulating the energy band structure, enhancing the separation of photogenerated carriers, and resulting in ROS generation (Fig. 1m). Furthermore, the fluorescence spectra of BFO and La-BFO were measured to investigate the electron-hole recombination behavior [30]. The emission peaks of La-BFO were weaker than those of BFO, which demonstrated the La doping-induced electron-hole separation capability (Fig. 1n).

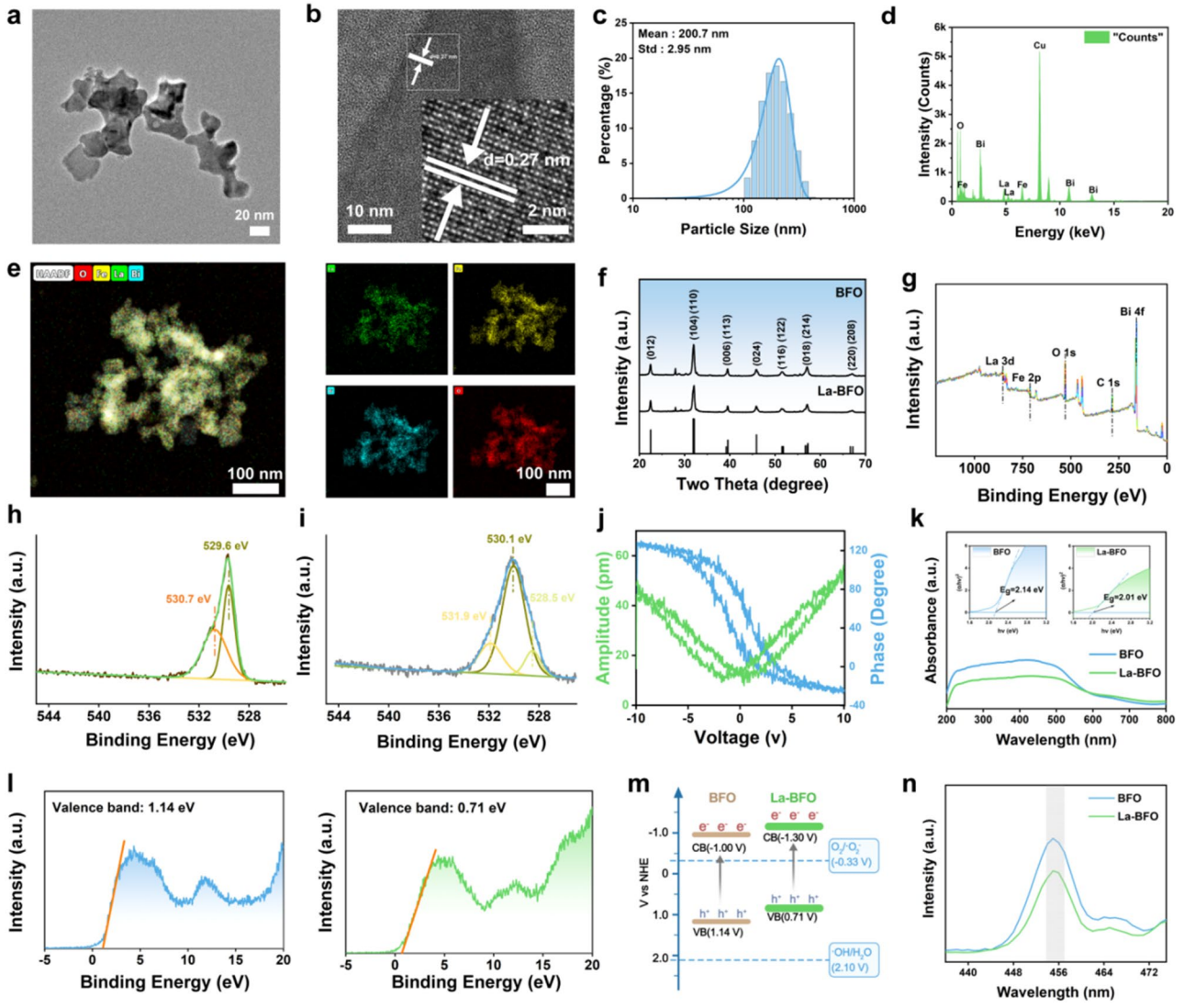

Fig. 1 (**a**) TEM image, (**b**) HRTEM image, (**c**) size distribution, (**d**) EDX spectrum of La-BFO. The Cu peak originates from the copper grid used for dispersing samples. (**e**) Element (La, Bi, Fe and O) mapping images of La-BFO. (**f**) X-ray diffraction pattern of BFO and La-BFO. (**g**) Wide-scan XPS spectrum of La-BFO. O 1s spectra of (**h**) BFO and (**i**) La-BFO. (**j**) Piezo-responsive amplitude curve and phase curve of La-BFO. (**k**) UV-vis absorption spectra and energy bandgap of BFO and La-BFO. (**l**) Valence XPS spectra of BFO (left) and La-BFO (right). (**m**) Energy band diagram of BFO (blue) and La-BFO (green). (**n**) Photoluminescence spectra of BFO and La-BFO

Theoretical calculations and multienzyme activities

Theoretical calculations were performed to investigate the effect of La doping on the piezoelectric properties of $BiFeO_3$. Given that La substitution and structural reconstruction could create oxygen vacancies, the structural optimization diagrams of BFO, La-BFO without oxygen vacancies ($BiFeO_3$-La), and La-BFO with oxygen vacancies ($BiFeO_3$-La-Ov) were constructed (Fig. 2a-c). The density of states (DOS) of BFO, $BiFeO_3$-La, $BiFeO_3$-La-Ov were calculated to investigate the defect states (Fig. 2d-f). Compared with BFO and La-BFO without oxygen vacancies, La-BFO with oxygen vacancies exhibited new defect states. The introduction of defects promotes the separation of electron-hole pairs. These calculation results suggested that La doping induced lattice distortion and formed defect bands, thus enhancing the piezoresponse.

Given the intimate association between valence variation characteristics of Fe ions and nanozyme-mimic activity, our investigation focused on determining whether the La-BFO nanocrystals feature nanozyme-mimicking activity. Being a hallmark feature of tumor tissues and a standard cellular antioxidant defense mechanism, overexpressed glutathione has been demonstrated to sequester ROS and hinder antitumor effects [31]. Therefore, the GPx-like activity, corresponding to the GSH consumption, was determined by measuring the change in nicotinamide adenine dinucleotide phosphate

hydride (NADPH). The decrease in characteristic absorbance at 340 nm indicated the GPx-like activity at the solution level (Fig. 2g). CAT, a renowned antioxidant nanozyme, catalyzes the conversion of H_2O_2 to O_2 to counteract the hypoxic tumor microenvironment. We assessed the CAT-mimicking activity by monitoring O_2 levels during the conversion of H_2O_2 to O_2. The dissolved oxygen meter indicated a rise in the oxygen content of La-BFO, positively correlated with the H_2O_2 amount (Fig. 2h), and the generation content of oxygen of La-BFO showed a greater increase than that of BFO (Fig S4), confirming the CAT-mimicking effect. Subsequently, the production of O_2 prompted us to verify the redox-mimicking activity. This activity primarily arises from the electron transfer pathway between La-BFO and oxygen, exhibiting substrate-like characteristics, leading to the generation of superoxide radicals ($\bullet O_2^-$). 3,3',5,5'-Tetramethylbenzidine (TMB) was used as a chromogenic substrate to assess $\bullet O_2^-$ production. As the concentration of La-BFO and TMB increased, the color transitioned from colorless to blue, accompanied by a gradual rise in peak intensity at 652 nm (Fig. 2i and Fig S5), demonstrating the OXD-mimicking activity of La-BFO.

Considering that high hydrogen peroxide (H_2O_2) content is a hallmark feature of the tumor microenvironment [32], the POD-mimicking activities of BFO and La-BFO nanocrystals using a TMB oxidation assay were measured, with H_2O_2 as an electron acceptor to evaluate

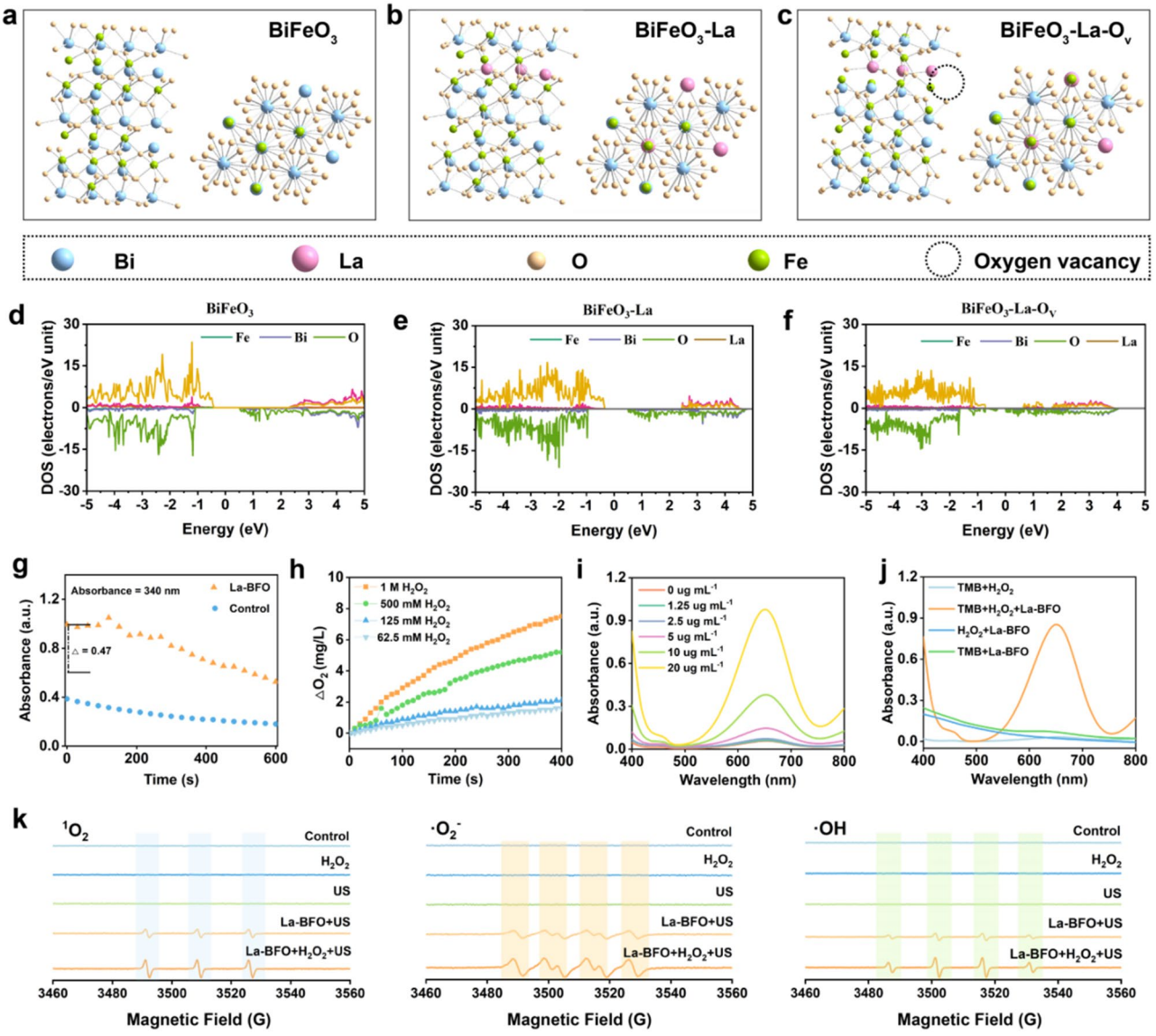

Fig. 2 Geometrically optimized structures of ideal (**a**) $BiFeO_3$, (**b**) $BiFeO_3$-La, and (**c**) $BiFeO_3$-La-Ov. Density of states (DOS) profiles of (**d**) $BiFeO_3$, (**e**) $BiFeO_3$-La, and (**f**) $BiFeO_3$-La-Ov. (**g**) GPx-like activity, (**h**) CAT-like activity, (**i**) OXD-like activity, and (**j**) POD-like activity of La-BFO. (**k**) ESR spectra of •OH and $\bullet O_2^-$ trapped by DMPO, $^1O_2$ trapped by TEMP

the generation of •OH. The setup of the TMB + H_2O_2 group was designed to eliminate the interference caused by the binding of the aforementioned substances. BFO/La-BFO + H_2O_2 + TMB groups produced obvious absorbance peaks at 652 nm (Fig. 2j and Fig S6), and the absorbance intensity is higher in the La-BFO-related group (Fig S7), demonstrating the positive effect of La doping on POD-like activity. In addition, the materials concentration, H_2O_2 content, and US time have a high influence on the reaction rate (Fig S8). The main ROS species produced with the assistance of US irradiation were subsequently quantitatively verified using typical electron spin resonance (ESR) assays (Fig. 2k). Corresponding spin traps to investigate the presence of ROS revealed typical ESR signals for DMPO-•OH, DMPO-•O_2^-, and TEMP-$^1O_2$ adducts [33, 34]. Characteristic signals of •OH, •O_2^- and $^1O_2$ emerged in the La-BFO + US and La-BFO + H_2O_2 + US groups. Methylene blue (MB) as a chromogenic substrate was further used for assessing the •OH production by a color change from blue to colorless [35]. La-BFO exhibited a more significant reduction in characteristic absorbance around 663 nm compared to BFO. This reduction became more pronounced with prolonged sonication time, providing further confirmation of the enhanced production of •OH upon US activation (Fig S9 and S10).

In vitro therapeutic efficacy

Considering the enhanced ROS generation ability of La-BFO at the solution level, we systematically investigated the therapeutic effect of La-BFO on 4T1 cancer cells in vitro. Polyvinyl pyrrolidone (PVP) modification on the surface of La-BFO was employed in the following cellular and animal experiments (Fig S11). The time-dependent uptake process of La-BFO was evaluated using a confocal laser scanning microscope (CLSM) (Fig. 3a). Also, the cellular uptake behavior of La-BFO using biological TEM was confirmed (Fig. 3b). The enhanced red fluorescence intensity of Rhodamine B-labelled La-BFO confirmed the occurrence of the internalization process, which is a fundamental requirement for the cytotoxic effect of La-BFO. The cytotoxicity of BFO and La-BFO towards 3T3 (mouse fibroblast) cells was minimal even at a high concentration of 200 μg mL^{-1}, demonstrating the high biocompatibility of La-BFO in vitro (Fig S12). Subsequently, we systematically assessed the factors influencing the cytotoxicity of La-BFO, such as H_2O_2, US power density, and dosage. The cytotoxicity of different concentrations of H_2O_2 on La-BFO cells is negligible (Fig. 3c). The decreased viability observed in La-BFO + US group at power levels up to 1.5 W cm^{-2} suggests that the US significantly amplifies the negative effect on cell proliferation, the cell killing rate reaches 88% (Fig. 3d). Also, the combination of La-BFO and US substantially improved the cell-killing effect (Fig. 3e). This is consistent with the results of Calcein-AM and PI double staining experiments (Fig. 3g and i).

To demonstrate the capacity of ROS generation by La-BFO to induce irreversible cell death, intracellular ROS production was assessed using the 2,7-dichlorofluorescein (DCFH-DA) probe (Fig. 3f, 3 h). Negligible fluorescence intensity was observed in 4T1 cells treated with H_2O_2, US, or La-BFO alone. Importantly, the introduction of additional H_2O_2 or US irradiation with La-BFO resulted in the induction of green fluorescence. Moreover, the La-BFO + H_2O_2 + US group exhibits the highest ROS generation compared to the other groups, thereby leading to US-enhanced ROS tumor therapy. Additionally, we validated the US enhanced GPx-like activity of La-BFO at the intracellular level using a glutathione peroxidase assay kit (Fig S13). Higher NADPH consumption in US + La-BFO group confirms the depletion of endogenous GSH.

Considering the close relationship between apoptosis and mitochondrial dysfunction (Fig. 3j), the changes in mitochondrial membrane potential in different groups were investigated by using 5,5',6,6'-tetrachloro-1,1',3,3'-tetraethyl-iodoimidocarbocyanine (JC-1) probe [36]. The polarization status of mitochondria can be ascertained based on the JC-1 probe, which demonstrates intact and ruptured mitochondrial membranes through the presence of red aggregates and green monomers, respectively. Consequently, alterations in mitochondrial membrane potential can be inferred by comparing the relative intensities of green and red fluorescence. The intensity ratio of green to red fluorescence increased in the La-BFO + H_2O_2, La-BFO + US, and La-BFO + H_2O_2 + US groups, relative to the La-BFO alone group. Specifically, the La-BFO + H_2O_2 + US group showed the most significant increase in intensity ratio and accompanying mitochondrial damage. No significant changes were observed in the groups that received specific treatments of H_2O_2 or US (Fig. 3k, 3 L). To further observe the mitochondrial damage, we utilized biological TEM to document the alterations in the mitochondria of the La-BFO + H_2O_2 + US group before and after treatment (Fig. 3b). The treatment resulted in significant mitochondrial structural damage, characterized by mitochondrial swelling, ridge breakage, and cavitation (red arrows and red circles).

RNA-sequencing and mechanism analysis

Transcriptome analysis was utilized to further elucidate the potential therapeutic mechanism of piezoelectric nanozyme on 4T1 cancer cells. The data points within the same treatment group showed significant clustering, underscoring the robust reliability of the RNA sequencing data (Fig S14). The heatmap revealed substantial

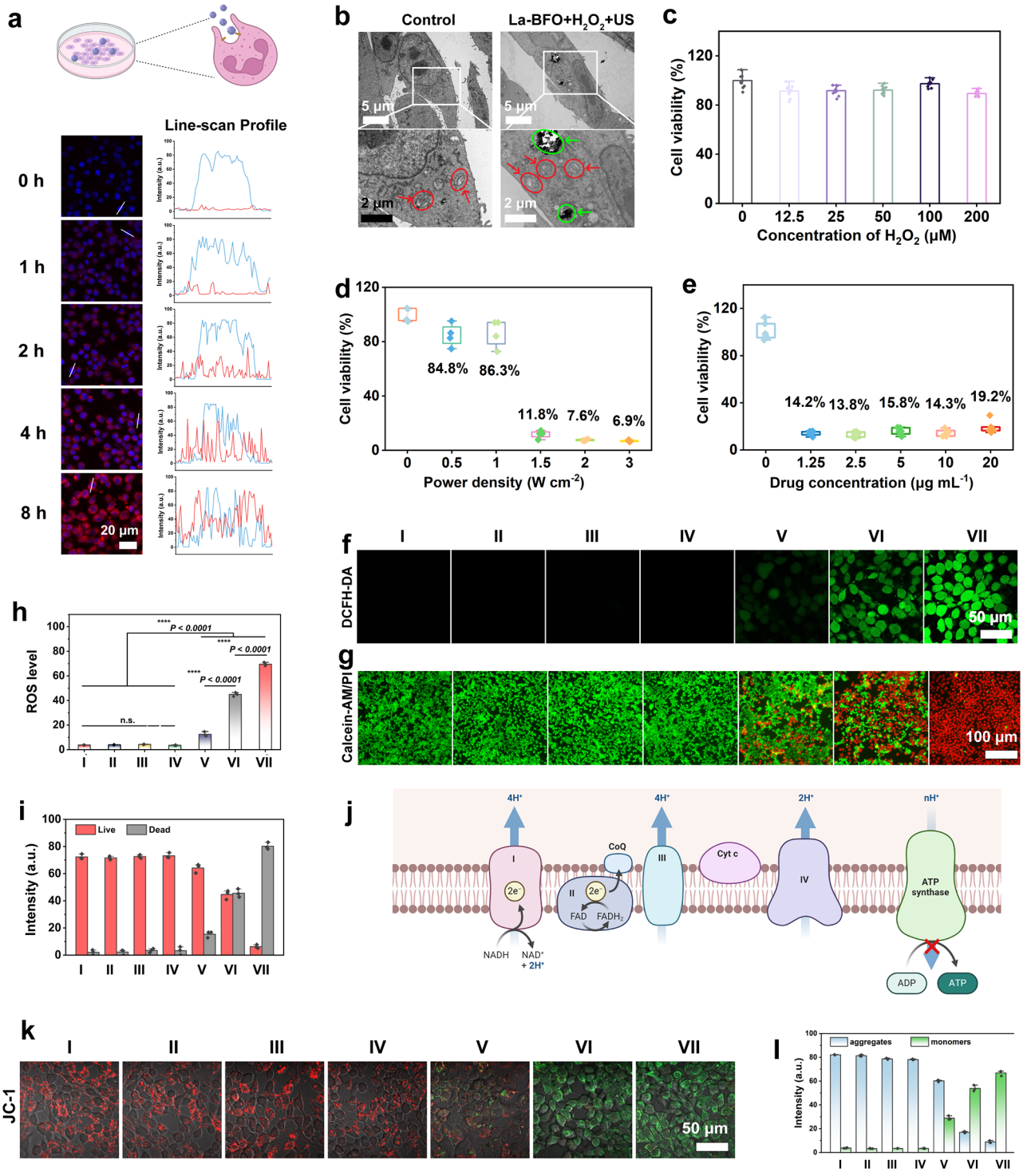

Fig. 3 (**a**) Confocal fluorescence images and the corresponding linear-scan profiles of 4T1 cells incubated with La-BFO (20 μg mL^{-1}) at different time intervals. (**b**) Bio-TEM images of 4T1 cells treated with control group and La-BFO + H_2O_2 + US group. (**c**) Cytotoxicity of different concentrations of H_2O_2 on 4T1 cells. (**d**) The cytotoxicity of La-BFO on 4T1 cells treated with US under different power densities (0, 0.5, 1, 1.5, 2 and 3 W cm^{-2}). (**e**) Cytotoxicity of different concentrations of La-BFO on 4T1 cells treated with US (1.5 W cm^{-2}). Representative CLSM images of (**f**) DCFH-DA staining and (**g**) Calcein AM/PI staining treated with different groups. The corresponding semi-quantitative analysis of (**h**) relative ROS levels and (**i**) live-dead levels. (**j**) Schematic illustration of destruction of mitochondrial membrane potential. Representative CLSM images of (**k**) JC-1 staining treated with different groups and (**l**) the corresponding semi-quantitative analysis of JC-1 aggregates and monomers (I: Control; II: H_2O_2; III: US; IV: La-BFO; V: La-BFO + H_2O_2; VI: La-BFO + US; VII: La-BFO + H_2O_2 + US). Statistical analyses were performed using one-way ANOVA. Data are expressed as mean ± standard deviation (SD), where $^*p < 0.05$, $^{**}p < 0.01$, $^{***}p < 0.001$, $^{****}p < 0.0001$, n.s: differences were not statistically significant

transcriptomic variances between the treatment and control groups. Specifically, the La-BFO + H_2O_2 + US group elicited 1320 differentially expressed genes, comprising 741 up-regulated and 579 down-regulated mRNAs (Fig S15-S17). Subsequently, a Kyoto Encyclopedia of Genes and Genomes (KEGG) analysis was performed (Fig S18). These findings indicated that differentially expressed genes (DEGs) linked to La-BFO treatment were predominantly enriched in interleukin-17 (IL-17), tumor necrosis factor (TNF), and NOD-like receptor signaling pathways, implying a strong connection between La-BFO treatment and inflammation induced by oxidative stress. Subsequently, we identified differentially expressed genes associated with IL-17, TNF, and NOD-like receptor signaling pathways through circus heat maps (Fig S19). Furthermore, the specific regulatory genes were visualized in the chordal plot of the KEGG pathway analysis (Fig. 4a), providing additional confirmation of the association between these DEGs and inflammation-related pathways. These findings suggest that La-BFO NPs play a critical role in modulating inflammation during breast cancer treatment.

Cellular pyroptosis is a novel type of programmed cell death that involves the significant release of pro-inflammatory factors. The cleavage of gastrin D protein (GSDMD) primarily defines this process. Furthermore, the NLRP3 inflammasome is widely recognized as a crucial regulator of pyroptotic cell death [7, 8]. The protein-protein interaction network of these inflammation-associated DEGs revealed that the dominant proteins included NLRP3, Casp1, and GSDMD, emerging as the key regulatory proteins (Fig. 4b). Therefore, a potential association could exist between pyroptosis and piezoelectric nanozyme-mediated cell death. Our objective was to integrate gene sequencing results to provide strong evidence supporting the induction of pyroptosis by La-BFO nanosystems. The strong inflammatory responses have been confirmed through IL-1β and lactic dehydrogenase (LDH) release (Fig. 4c and d). In pursuit of this objective, we commenced with cell morphology observation as the primary and intuitive methodology. 4T1 cancer cells treated with BFO/La-BFO + H_2O_2 + US groups exhibited bubble and swelling features, which initially confirmed the occurrence of pyroptosis. Most importantly, the increased formation of gastrin D pores validated the significant role of La ions in triggering pyroptosis in cancer cells (Fig. 4e). Acridine orange staining experiments were conducted to assess the impact of La-BFO on lysosomal integrity. Normal lysosomes exhibited an orange-yellow color, with this fluorescence significantly reduced following treatment in the La-BFO + H_2O_2 + US group (Fig. 4g). The La ions can react with the phosphate groups on the lysosomal membrane, disrupting the lysosomal membrane and amplifying the pyroptosis effect (Fig. 4f) [24]. Western blot analysis and correlation quantification were used to assess protein expression and determine the activation of the NLRP3 inflammasome and Caspase-1, which leads to the cleavage of GSDMD into N-GSDMD. The enhanced expression of NLRP3, cleaved Caspase-1 and N-GSDMD affirmed the synergistic effect of ROS and La ions (Fig. 4h-i). Subsequently, we performed typical flow apoptosis experiments by staining 4T1 cancer cells with annexin V-FITC and PI (Fig. 4j). In the La-BFO + H_2O_2 + US-treated group, the percentage of apoptosis (sum of Q2 and Q3) in 4T1 cancer cells reached 61.65%, significantly exceeding that of the control group. The above results indicate that both pyroptosis and apoptosis occur simultaneously in the La-BFO-related groups. Considering that pyroptosis is a cell death pathway that facilitates cancer immunotherapy, the immunofluorescence staining experiments have been applied to detect the expression of immunogenic cell death biomarkers, surface-exposed calreticulin (CRT). It can be revealed that the US-triggered La-BFO treatment group significantly led to changes in the expression of CRT (Fig S20).

MRI/CT dual-modal imaging

Due to the high X-ray attenuation coefficient of Bi [37], La-BFO has the potential to serve as an effective contrast agent for computed tomography (CT) imaging, facilitating treatment guidance. Figure 5a and b shows the CT images and corresponding CT values for La-BFO solutions at concentrations of 0, 0.5, 1, 2, 4, 8, and 16 mg mL^{-1}, respectively. As the concentrations of La-BFO increased, the grey scale of the images shifted towards a brighter appearance, the yellowish pseudo-color images gradually transformed into a vibrant red hue, and the Hounsfield unit values exhibited concentration-dependent characteristics. The measured CT signals exhibited a linear positive correlation with the fitted curves of La-BFO concentration, suggesting that La-BFO is an effective contrast agent with promising CT imaging capabilities. Acknowledging the significant CT efficacy demonstrated by La-BFO, we evaluated its viability as an in vivo CT contrast agent. For in vivo imaging, La-BFO was administered through the mice's tail vein, and subsequent CT imaging was performed at various time intervals (0, 0.5, 1, 1.5, 2, 2.5 h). The CT signals at the tumor site showed gradual enhancement over time, with peak brightness observed one hour after injection (Fig. 4c and d). One hour post-intratumoral injection, the CT signal displayed a substantial enhancement relative to the pre-injection baseline, which was validated by the corresponding CT cross-sectional line profiles (Fig S21).

The presence of iron in La-BFO enables it to be utilized for clinical diagnosis and monitoring of the accumulation of La-BFO in the tumor area, as Fe-based materials can serve as a T_2-weighted MRI contrast agent [38]. The

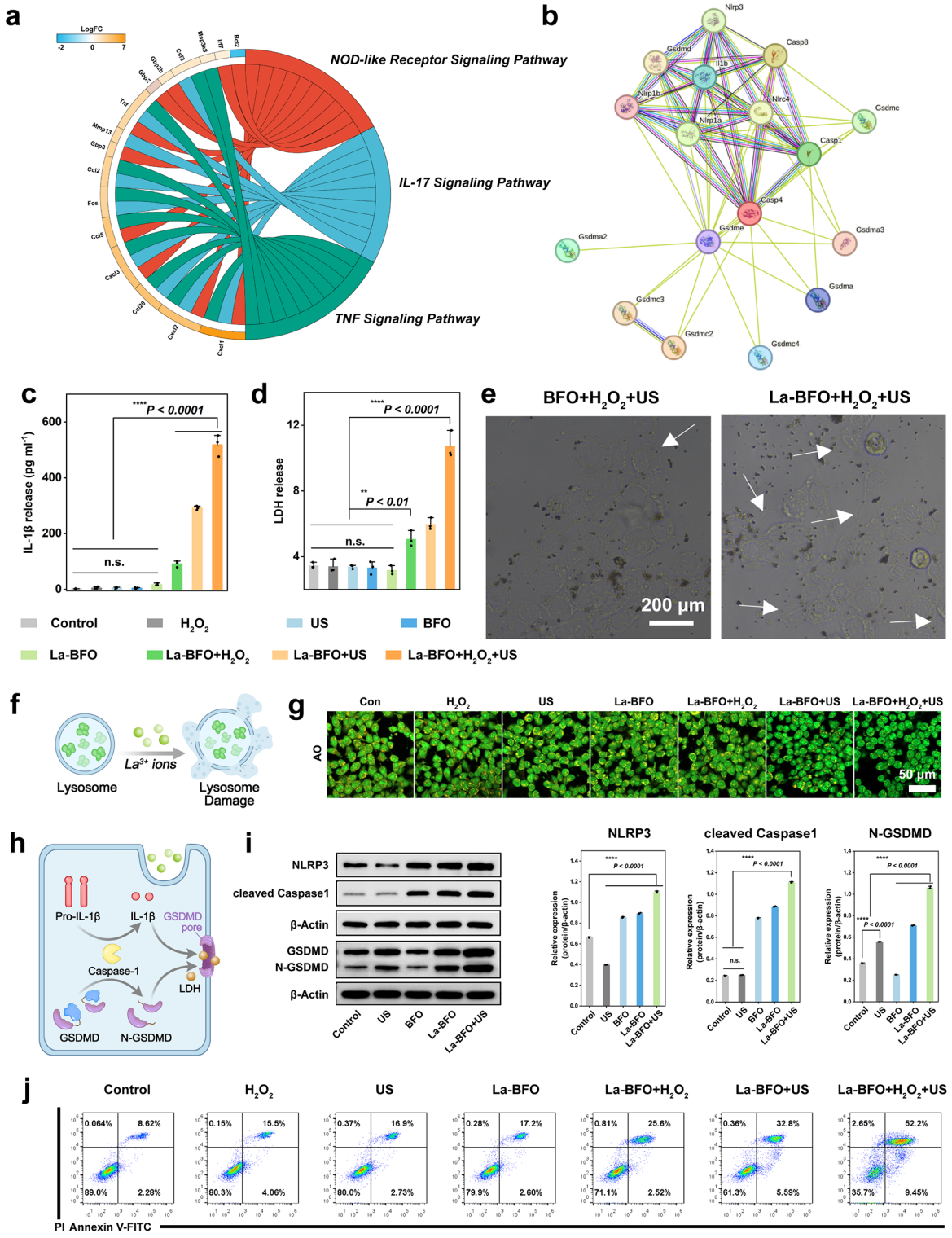

Fig. 4 (**a**) Enriched KEGG pathway chordal map based on the intersection of three pathways (NOD-like Receptor Signaling Pathway; IL-17 Signaling Pathway; TNF Signaling Pathway). (**b**) Protein-protein interaction network of these functional genes. (**c**) IL-1β ($n = 3$) and (**d**) LDH release ($n = 3$) after being treated with different groups. (**e**) Morphological features of 4T1 cancer cells in control, BFO + H_2O_2 + US and La-BFO + H_2O_2 + US groups. White arrows represent swollen cells with large air bubbles. (**f**) Schematic diagram of lysosomal disruption by La ion. (**g**) Confocal fluorescence images of AO staining of 4T1 cells after different treatments. (**h**) Diagram of pyroptosis pathway. (**i**) Western blot analysis of NLRP3, cleaved Caspase-1, GSDMD, N-GSDMD in 4T1 cells and the corresponding quantitative analysis ($n = 3$) after varied treatments. (**j**) Annexin V-FITC and PI staining assay of 4T1 cells after different treatments. Statistical analyses were performed using one-way ANOVA. Data are expressed as mean ± standard deviation (SD), where $^{*}p < 0.05$, $^{**}p < 0.01$, $^{***}p < 0.001$, $^{****}p < 0.0001$, n.s: differences were not statistically significant

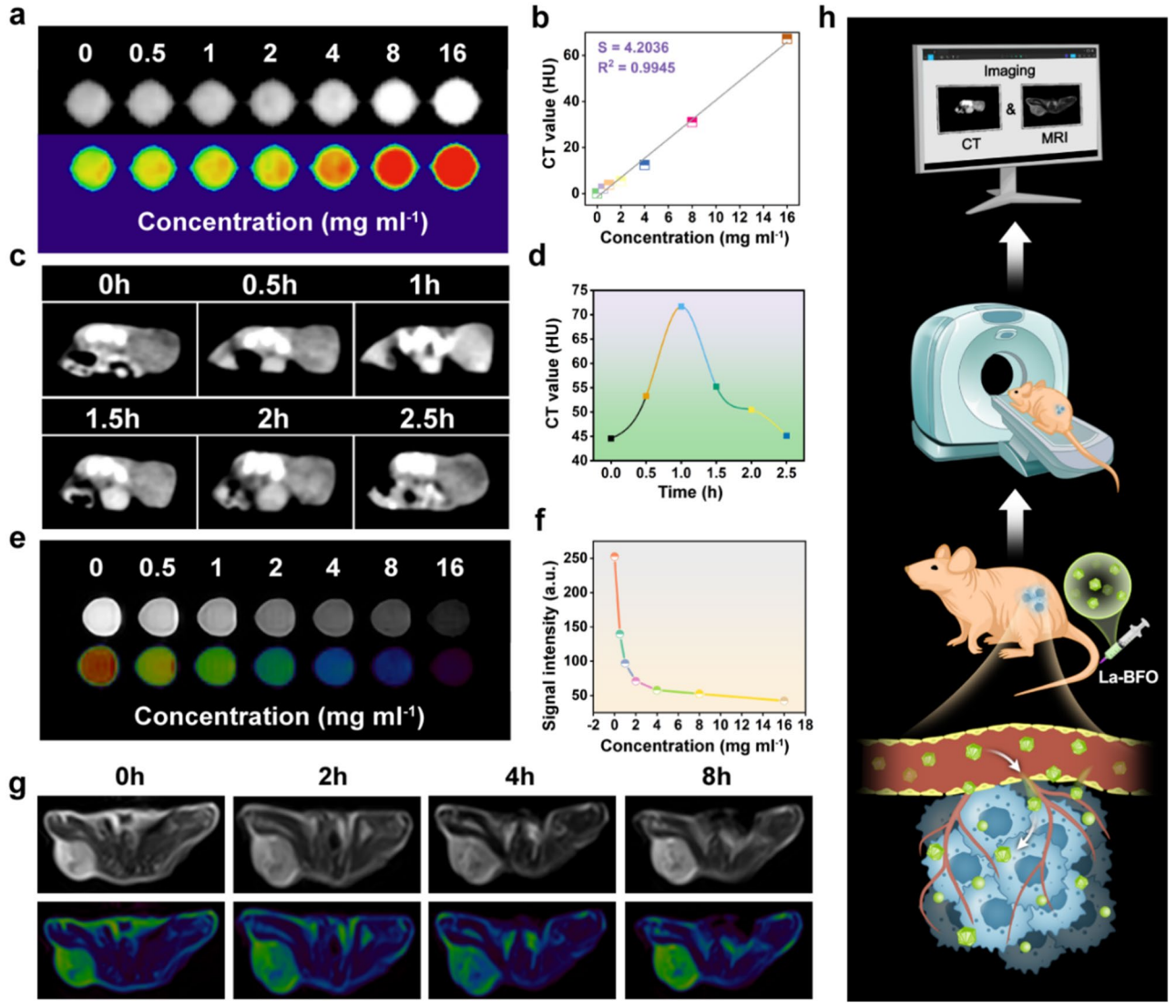

Fig. 5 (**a**) CT images of different concentrations of La-BFO solutions. (**b**) X-ray attenuation of intensity in Hounsfield units (HU) of La-BFO as a function of concentration. (**c**) In vivo CT images were captured at 0, 0.5, 1, 1.5, 2, and 2.5 h after intravenous administration of La-BFO (10 mg kg^{-1}). (**d**) The average intensity of CT signals from the tumor after intravenous administration at different times. (**e**) MRI images of different concentrations of La-BFO solutions. (**f**) In vitro T_2 signaling intensity of La-BFO with different concentrations. (**g**) In vivo MRI images were captured at 0, 2, 4 and 8 h after intravenous administration of La-BFO (10 mg kg^{-1}). (**h**) Schematic of in vivo imaging

T_2-weighted MRI performance of La-BFO solutions with varying concentrations (0, 0.5, 1, 2, 4, 8, and 16 mg mL^{-1}) was analyzed using a 3.0 T clinical MRI scanner (Fig. 4e). As the concentration increases, the changes in image darkness become apparent, accompanied by a gradual transition in pseudo-color maps from orange-red to dark purple. In addition, the in vitro quantification of T_2-MRI brightness demonstrated a reduction in image intensity as the concentration of La-BFO increased (Fig. 4f). The MRI signal at the tumor site exhibited a gradual decrease over time, reaching its lowest intensity at 4 h, indicating the in vivo MRI imaging ability of La-BFO (Fig. 4g h).

In vivo therapeutic efficacy

Due to the efficient cellular uptake and excellent in vitro therapeutic properties of La-BFO, the anticancer properties were evaluated in vivo. Firstly, the biocompatibility of La-BFO was assessed in vivo. The hematological parameters, including alkaline phosphatase (ALP), alanine aminotransferase (ALT), aspartate aminotransferase (AST), urea (UREA), creatinine (CRE), white blood cells (WBC), red blood cells (RBC), and platelets (PLT) in the La-BFO group did not show significant differences compared to the control group (Fig S22). Hematoxylin-eosin (H&E) staining of major organs (heart, liver, spleen, lungs, and kidney) demonstrates excellent biocompatibility and biosafety at the administered dose (Fig S23).

The biodistribution of La-BFO was further analyzed by in vivo fluorescence imaging. La-BFO nanoparticles, labeled with Cy5.5, were intravenously injected (Fig S24). La-BFO nanoparticles are primarily enriched in the liver of mice. Furthermore, ICP-MS results further confirmed the biodistribution of La-BFO nanoparticles in mice (Fig S25). We subsequently assessed the anticancer properties of piezoelectric nanozyme on subcutaneous tumors in 4T1 tumor-bearing nude mice. Thirty female mice, each with an approximate tumor volume of 100 mm^3, were selected and randomly divided into six groups ($n = 5$), including (1) PBS group, (2) US group, (3) La-BFO group (intravenously; *i.v.*), (4) La-BFO group (intratumorally; *i.t.*), (5) La-BFO (*i.v.*) + US group, and (6) La-BFO (*i.t.*) + US group. 10 mg kg^{-1} of La-BFO was administered on days 1, 3, 5, and 7 followed by US irradiation (1.0 MHz, 1.5 W cm^{-2}, 50% duty cycle, 1 min, five cycles) 6 h later (Fig. 6a). There were no significant differences observed in the mean body weight among each group (Fig. 6b). Subsequently, the tumor volume was monitored and verified, highlighting the significant role of ultrasound in achieving a higher tumor inhibition rate in the La-BFO + US group compared to the La-BFO group. The highest level of inhibition was observed in the La-BFO *i.t.* + US group, where the average tumor volume in mice was measured to be 226 mm^3 (Fig. 6c). By the end of day 14, ths La-BFO *i.t.*+ US group showed a 76.7% tumor inhibition rate, surpassing the rates observed in the US group (8.3%), the La-BFO *i.v.* group (37.8%), the La-BFO *i.t.* group (38.8%) and the La-BFO *i.v.* + US group (73.9%) (Fig. 6d). The weight of the isolated tumors was consistent with the growth data (Fig S26). Subsequently, H&E staining of tumor sections was performed to assess the extent of cell damage and necrosis (Fig. 6e). The 4T1 cells in the control and US alone groups maintained a normal morphology, while those in the La-BFO *i.v.* and La-BFO *i.t.* groups displayed slight damage. In contrast, the La-BFO *i.v.*+ US and La-BFO *i.t.*+ US groups exhibited typical histopathological damage.

Tumor proliferation behavior was monitored through Ki67 immunohistochemical staining (Fig. 6f). The reduced expression of Ki67 in the La-BFO *i.v.* + US group and La-BFO *i.t.* + US group demonstrated the effective inhibitory effect. Moreover, the terminal deoxynucleotidyl transferase-mediated dUTP nickel end labeling (TUNEL) assay affirmed the highest cellular apoptotic degree caused by the US-amplified piezoelectric nanozyme (Fig. 6g). The expression of proteins associated with pyroptosis was detected using in vivo immunofluorescence analysis. Increased expression of cleaved Caspase-1 (Fig. 6h-i) and N-GSDMD (Fig. 6j-k) could be detected in tumor sections treated with La-BFO *i.v.* + US group and La-BFO *i.t.* + US group, confirming the occurrence of pyroptosis. Previous studies have suggested that pyroptosis is a cell death mechanism that enhances cancer immunotherapy. Therefore, we developed a primary distal tumor model to validate its inhibitory effects on both primary and metastatic tumors. In comparison to the control group, the La-BFO + US group exhibited significant inhibition of both primary and metastatic tumors (Fig S27).

Conclusions

In summary, La-BFO piezoelectric nanozymes were rationally designed and engineered for inducing pyroptosis of breast cancer cells by the US-activated sonopiezoelectric effect. The lanthanum-doping strategy effectively narrowed the band gap of BFO and introduced oxygen vacancies, thereby enhancing ROS generation efficiency by reducing the recombination rate of electron-hole pairs. The release of La ions potently disrupted the lysosomal membrane, amplifying the effect of pyroptotic cell death. The RNA sequencing results unequivocally confirmed the role of ROS activation and the La^{3+}-induced Caspase-1/GSDMD pathway in the pyroptosis-related anti-tumor mechanism. Both in vitro and in vivo experiments confirmed the CT/MRI dual-mode imaging capacity and prominent antineoplastic results. This work presents a paradigm for engineering high-performance piezoelectric materials through specific element doping and vacancy creation, achieving tumor pyroptosis-based nanotherapy.

Materials and methods

Materials

$Fe(NO_3)_3{\cdot}9H_2O$, $La(NO_3)_3{\cdot}6H_2O$, $Bi(NO_3)_3{\cdot}5H_2O$, ethylene glycol, HNO_3, and polyvinylpyrrolidone (PVP), 3,3′,5,5′- Tetramethylbenzidine dihydrochloride hydrate (TMB), methylene blue (MB) were obtained from Aladdin (Shanghai, China). 5,5-dimethyl-1-pyrroline n-oxide (DMPO) and 2,2,6,6-Tetramethyl-4-piperidone hydrochloride (TEMP) were bought from Dojindo (Dojindo, China). CCK-8 viability assay kit, Calcein/PI Cell Viability/Cytotoxicity Assay Kit, JC-1 Mitochondrial Membrane Potential Assay Kit, Annexin V-FITC/PI Kit, the BCA Protein Assay Reagent Kit, were purchased from Beyotime Biotechnology (Shanghai, China). Acridine Orange staining assay was purchased from Sigma-Aldrich (California, USA). PBS, RPMI 1640 medium, penicillin/streptomycin and fetal bovine serum (FBS) were bought from YoBiBiotech Co., Ltd.

Synthesis of BFO piezoelectric nanozyme

BFO piezoelectric nanozyme was prepared via a sol-gel method with a special air-quenching process. In brief, 2 mmol $Bi(NO_3)_3{\cdot}5H_2O$ and 2 mmol $Fe(NO_3)_3{\cdot}9H_2O$ were dispersed in ethylene glycol (20 ml). After adjusting the pH value of the solution to 3–4 with HNO_3, the mixture

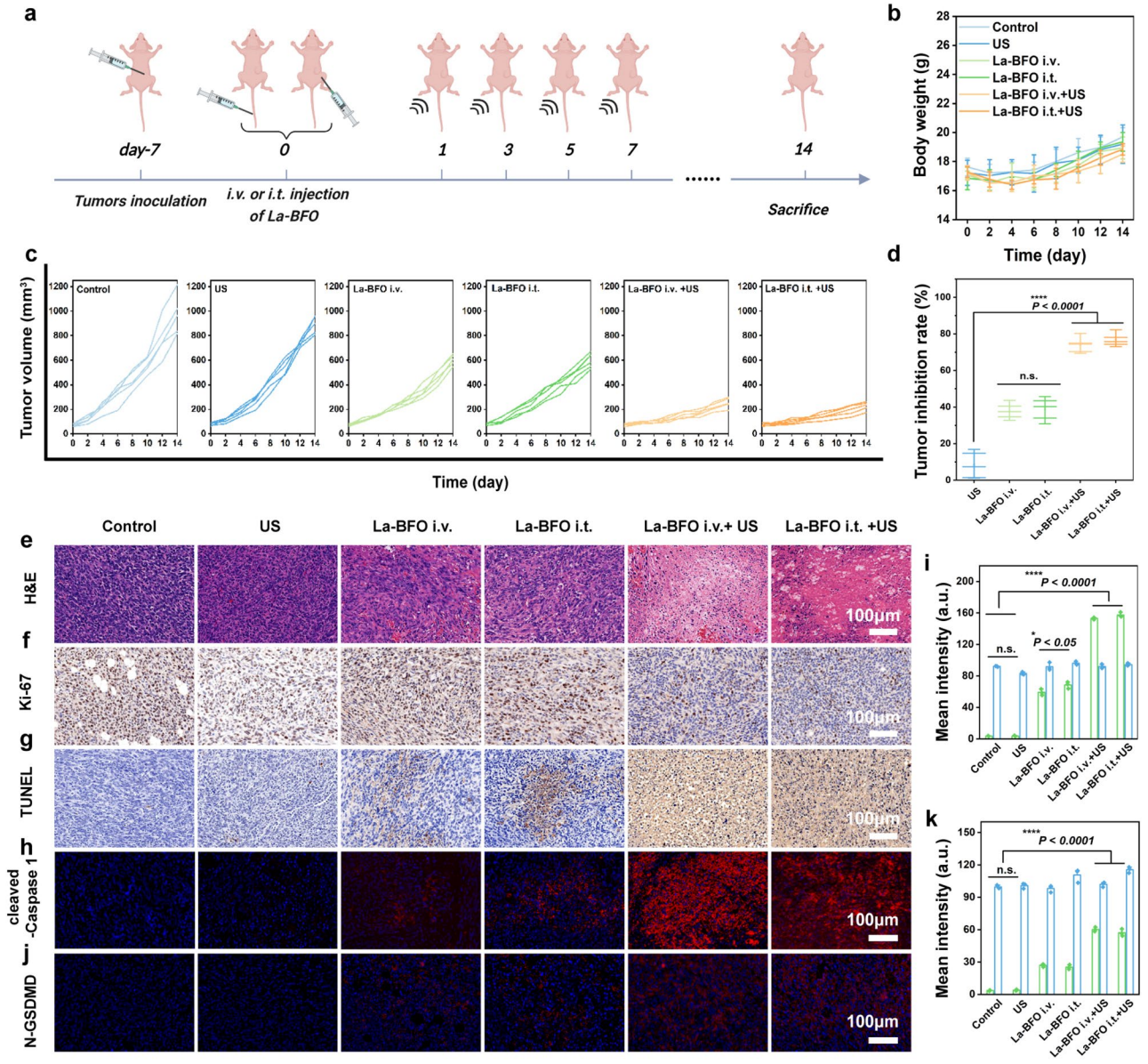

Fig. 6 (**a**) Schematic diagram of the schedule of in vivo anticancer treatment. (**b**) Body weight changes. (**c**) Individual tumor growth curves of 4T1 nude mice treated with different groups ($n = 5$). (**d**) Tumor inhibition rate in mice after different treatments ($n = 5$). (**e**) H&E, (**f**) Ki-67, (**g**) TUNEL staining images of tumor slices from tumor-bearing mice treated with various treatments. (**h**) cleaved Caspase 1, (**j**) N-GSDMD staining images and (**i**, **k**) the corresponding fluorescence semi-quantitative results of tumor slices from the tumor-bearing mice in different treatment groups. Statistical analyses were performed using one-way ANOVA. Data are expressed as mean ± standard deviation (SD), where $^{*}p < 0.05$, $^{**}p < 0.01$, $^{***}p < 0.001$, $^{****}p < 0.0001$, n.s: differences were not statistically significant

was heated at 70 ℃ for 2 h to form the sol, followed by additional heating at 120 ℃ for 6 h to obtain the gel. The as-obtained gel was initially calcined at 400 ℃ for 20 min to eliminate nitrates from the system, and the resulting products were finely ground after cooling naturally to room temperature. Ground powders were calcined in a muffle furnace at 500 ℃ for 60 min.

Synthesis of La-BFO piezoelectric nanozyme

Firstly, 1.8 mmol $Bi(NO_3)_3{\cdot}5H_2O$, 2 mmol $Fe(NO_3)_3{\cdot}9H_2O$ and 0.2 mmol $La(NO_3)_3{\cdot}6H_2O$ were respectively dissolved in 20 ml ethylene glycol to obtain a mixed solution. Twenty microliters of nitric acid were added to dissolve and present a clear solution, then the mixed homogeneous solution was stirred at 80 ℃ for 1 h and dried at 100 ℃ overnight to obtain a precursor gel. After grinding the gel into powder, the precursor powder was calcined at 500 ℃ for 2 h to obtain the catalyst.

ESR measurement

ESR experiments were performed with the assistance of the trapping agent DMPO (Dojindo-D048, China Co., Ltd.) and TEMP (Dojindo-T511, China Co., Ltd.). For La-BFO samples, 100 μL La-BFO (5 mg mL^{-1}), 1 μL H_2O_2 (10 M), 900 μL PBS buffer or methanol solutions were mixed with 20 μL DMPO or TEMP under US irradiation (1.5 W cm^{-2}, 50% duty cycle, 1 min). Then •OH with the characteristic 1:2:2:1 signals (DMPO-PBS buffer), $•O_2^-$ with 4 large and 2 small characteristic signals (DMPO-methanol) and $^1O_2$ with the characteristic 1:1:1 signals (TEMP-PBS buffer) were detected by an electron paramagnetic resonance spectrometer.

Glutathione peroxidase (GPx)-mimicking activity of La-BFO

The GPx-like activity of La-BFO was determined using a GPx assay kit (Beyotime Biotechnology) according to a standard protocol. In the presence of H_2O_2 (50 mM) and La-BFO (200 μg mL^{-1}), glutathione (GSH, 7.5 mM) underwent oxidation to form L-glutathione oxidation (GSSG), and then GSSG was reduced to GSH by glutathione reductase (GR) in the presence of NADPH (0.625 mM). The absorbance of the mixtures was measured by a microplate reader (absorbance at 340 nm).

Catalase (CAT)-mimicking activity of La-BFO

The CAT-like activity of La-BFO was evaluated by detecting the O_2 generation with a dissolved oxygen meter (INESA Scientific Instrument, Shanghai). Typically, 100 μg ml^{-1} La-BFO was added into H_2O with different concentrations of H_2O_2 (62.5 mM, 125 mM, 500 mM, 1 M), and the oxygen concentration (mg L^{-1}) was immediately recorded for 400 s.

Oxidase (OXD)-mimicking activity of La-BFO

The OXD-like activity of La-BFO was determined using TMB as substrate. La-BFO was mixed with TMB in ultrapure water. The total amount of the entire system is 3 mL. The change in absorbance of the reaction solution at 652 nm was determined by a UV-Vis-NIR spectrophotometer. Experimental variables included La-BFO concentration (0, 1.25, 2.5, 5, 10, 20 μg mL^{-1}) and TMB concentration (0, 0.5, 1, 2, 4, 8 mM).

Peroxidase (POD)-mimicking activity of La-BFO

The POD-mimic activity of La-BFO was measured using TMB as the substrate in the presence of H_2O_2. In a typical process, 0.8 mM TMB, 1 mM H_2O_2 and 100 μg mL^{-1} La-BFO were mixed in the PBS solution. The total amount of the entire system is 3 mL. The absorbance was recorded after a certain reaction time using a UV-vis spectrophotometer and microplate reader (absorbance at 652 nm). The experimental variables included the concentrations of La-BFO (0, 0.02, 0.04, 0.06, 0.08, 0.1 mg mL^{-1}), H_2O_2 (0, 1, 2, 4, 6, 10 mM), and different US irradiation time (0, 30, 60, 120 s).

MB degradation

The ROS generation during the ultrasonic process was detected by the degradation of MB. 3 mg of BFO or La-BFO were dispersed in 3 mL MB aqueous solution (2 mg L^{-1}). In order to study the degradation effect of BFO or La-BFO on MB under US irradiation (1.0 MHz, 1.5 W cm^{-2}, 50% duty cycle), the mixture was centrifuged to take the supernatant for measurement every 1 min of sonication, and the supernatant was mixed with the precipitate after the measurement, and the time points of sonication were 1, 2, 3, 4, 5 and 6 min, and the supernatant was analyzed with UV-visible absorption spectroscopy.

Preparation of La-$BiFeO_3$-PVP (La-BFO@PVP)

10 mg of La-BFO powder was dissolved in 10 ml of deionized water, then 100 mg of PVP was added and stirred for 24 h. Finally, the final product was washed repeatedly with water and ethanol.

Cell culture

4T1 (mouse breast cancer cells) were purchased from the Cell Bank of Shanghai Institute of Biochemistry and Cell Biology, Chinese Academy of Sciences. Cells were cultured in DMEM medium supplemented with 10% fetal bovine serum and 1% penicillin/streptomycin at 37 °C in a humidified atmosphere with 5% CO_2.

Bio-TEM observation

4T1 cells were seeded in 6-well plates and cultured for 24 h up to 70–80% confluence. Cells were treated with different groups and incubated for 24 h. Subsequently, the treated cells were collected, centrifuged and resuspended in 2.5% glutaraldehyde fixative overnight. After fixation in osmium tetroxide solution for 1 h at room temperature, the cells were then dehydrated with gradient ethanol solutions and embedded in resin. The prepared sections were imaged by TEM.

Cellular uptake

4T1 cells were seeded in a confocal glass bottom-dish (cell density = 10^5 cells per disk) and cultured. Then the cell culture medium was replaced with fresh culture medium containing rhodamine B-labeled La-BFO (20 μg mL^{-1}) for 0, 1, 2, 4 and 8 h, respectively. The treated 4T1 cells were washed twice with PBS for confocal laser scanning microscope (CLSM) observation.

In vitro cytotoxicity assay

4T1 cells were inoculated in 96-well plates (cell density = 10^4 cells per disk) and cultured for 24 h. Then, the

cells were treated with a mixture containing different concentrations of La-BFO (0, 1.25, 2.5, 5, 10, and 20 μg mL^{-1}), different concentrations of H_2O_2 (0, 12.5, 25, 50, 100, and 200 μM). and different US powers (0, 0.5, 1, 1.5, 2, and 3 W cm^{-2}) treatments have been applied. Finally, a CCK-8 assay was performed.

Detection of intracellular ROS production

4T1 cells were seeded in a confocal glass bottom dish (cell density = 10^5 cells per disk) and cultured for 24 h. Then, 4T1 cells were treated with the following conditions: (1) Control; (2) H_2O_2; (3) US (1.5 W cm^{-2}, 50% duty cycle, 1 min); (4) La-BFO (20 μg mL^{-1}); (5) La-BFO + H_2O_2 (100 μM); (6) La-BFO + US; (7) La-BFO + H_2O_2 + US. After co-incubation at 37 °C for 4 h, the US-related groups were exposed to the US irradiation, and then DCFH-DA (10 μM) was added followed by an additional 40 min incubation in the dark. Cells were washed twice with PBS after different treatments for CLSM observation.

Detection of live/dead cells

4T1 cells were seeded in a confocal glass bottom dish (cell density = 10^5 cells per disk) and cultured for 24 h. Then, 4T1 cells were treated with the following conditions: (1) Control; (2) H_2O_2; (3) US (1.5 W cm^{-2}, 50% duty cycle, 1 min); (4) La-BFO (20 μg mL^{-1}); (5) La-BFO + H_2O_2 (100 μM); (6) La-BFO + US; (7) La-BFO + H_2O_2 + US. After co-incubation at 37 °C for 8 h, the cells were co-incubated with Calcein AM and PI for 30 min. Finally, 4T1 cells were washed repeatedly with PBS and then imaged using a fluorescence microscope.

Cell apoptosis analysis

4T1 cells were seeded in 6-well plates and cultured for 24 h up to 70–80% confluence. 4T1 cells were treated with the following conditions: (1) Control; (2) H_2O_2; (3) US (1.5 W cm^{-2}, 50% duty cycle, 1 min); (4) La-BFO (20 μg mL^{-1}); (5) La-BFO + H_2O_2 (100 μM); (6) La-BFO + US; (7) La-BFO + H_2O_2 + US, and incubated for 24 h. Then, 4T1 cells were double stained with the Annexin V-FITC Apoptosis Detection Kit (Beyotime-C1062S, Shanghai, China) followed by the flow cytometric analysis.

In vitro GSH depletion

Intracellular glutathione depletion of La-BFO was indirectly determined using a glutathione peroxidase assay kit. Firstly, 4T1 cells were treated in the control group, US group (1.5 W cm^{-2}), La-BFO group (20 μg mL^{-1}) and La-BFO + US group, and the required reagents were added sequentially according to the steps in the instruction manual, and the intracellular glutathione of La-BFO was determined indirectly by measuring the absorbance at 340 nm by a microplate reader.

Lysosomal disruption analysis

4T1 cells were seeded in a confocal glass bottom dish (cell density = 10^5 cells per disk) and cultured for 24 h. Then, 4T1 cells were treated with the following conditions: (1) Control; (2) H_2O_2; (3) US (1.5 W cm^{-2}, 50% duty cycle, 1 min); (4) La-BFO (20 μg mL^{-1}); (5) La-BFO + H_2O_2 (100 μM); (6) La-BFO + US; (7) La-BFO + H_2O_2 + US. After co-incubation at 37 °C for 8 h, the cells were co-incubated with acridine orange (AO) (10 μM) for 30 min. Finally, 4T1 cells were washed repeatedly with PBS and then imaged using CLSM.

Detection of mitochondrial membrane potential

4T1 cells were seeded in a confocal glass bottom dish (cell density = 10^5 cells per disk) and cultured for 24 h. Then, 4T1 cells were treated with the following conditions: (1) Control; (2) H_2O_2; (3) US (1.5 W cm^{-2}, 50% duty cycle, 1 min); (4) La-BFO (20 μg mL^{-1}); (5) La-BFO + H_2O_2 (100 μM); (6) La-BFO + US; (7) La-BFO + H_2O_2 + US and incubated for 4 h. The US-related groups were exposed to the US irradiation and co-incubation at 37 °C for another 4 h. Then, 4T1 cells were stained with the mitochondrial membrane potential assay kit (Beyotime-C2006, Shanghai, China).

mRNA sequencing and analysis

4T1 cells treated with control the group and La-BFO (20 μg mL^{-1}) + H_2O_2 (100 μM) + US (1.5 W cm^{-2}, 50% duty cycle, 1 min) group were collected using Trizol (Invitrogen) for mRNA sequencing and analysis. The mRNA high-throughput sequencing was performed in Personal Biotechnology Co., Ltd. Shanghai, China. The data were analyzed online by using the free platform Personalbio GenesCloud (https://www.genescloud.cn)*.

Lactic dehydrogenase (LDH) assays

4T1 cells were seeded into 96-well plates and cultured for 24 h. Then, 4T1 cells were treated with the following conditions: (1) Control; (2) H_2O_2; (3) US (1.5 W cm^{-2}, 50% duty cycle, 1 min); (4) BFO (20 μg ml^{-1}); (5) La-BFO (20 μg ml^{-1}); (6) La-BFO + H_2O_2 (100 μM); (7) La-BFO + US; (8) La-BFO + H_2O_2 + US and incubated. The release of LDH was detected by the Mouse LDH Elisa Kit (U96-3563E) according to the manufacturer's protocols.

Interleukin-1β (IL-1β) secretion

4T1 cells were seeded into 96-well plates and cultured for 24 h. Then, 4T1 cells were treated with the following conditions: (1) Control; (2) H_2O_2; (3) US (1.5 W cm^{-2}, 50% duty cycle, 1 min); (4) BFO (20 μg ml^{-1}); (5) La-BFO (20 μg ml^{-1}); (6) La-BFO + H_2O_2 (100 μM); (7) La-BFO + US; (8) La-BFO + H_2O_2 + US and incubated. The release of IL-1β was detected by the Mouse IL-1β ELISA kit (Yubi (shanghai) Trading Co, LTD).

Western blot analysis

4T1 cells were seeded in 6-well plates and cultured for 24 h up to 70–80% confluence. Cells were treated with different groups (1. Control; 2. US (1.5 W cm^{-2}, 50% duty cycle, 1 min); 3. La-BFO (20 μg mL^{-1}); 4. La-BFO (20 μg mL^{-1}) + US) and incubated for 8 h, the treated cells were washed with PBS and lysed to collect the protein. The PVDF membranes were blocked with 5% nonfat dry milk at room temperature for 1 h in the decoloring shaker. Then incubated with anti-GSDMD (EPR19828, Abcam), anti-cleaved-Caspase 1 (Ala317), anti-NLRP3 (EPR23094-1, Abcam) overnight at 4 °C. The membranes were washed three times in the decoloring shaker. Then the membranes were incubated with secondary antibodies for 30 min and washed for three times in the decoloring shaker. The electrochemiluminescence reagent was added and reacted for 1–2 min. The membranes were exposed in a darkroom. Finally, the protein expressions were quantified by the software Image J.

Immunofluorescence staining

The CRT exposure was detected using immunofluorescence staining. 4T1 cells were seeded in a confocal glass bottom dish (cell density = 10^5 cells per disk) and cultured for 24 h. Cells were treated with different groups (La-BFO concentration of 20 μg mL^{-1}, US: 1.2 W, 1.5 min) and incubated for 12 h. Then, the cells were fixed for 10 min with 4% paraformaldehyde, and permeabilized for 10 min with 0.1% Triton X-100. After that, the cells were blocked with 5% BSA for 20 min before being treated overnight with anti-CRT antibody. Fluorescent secondary antibody incubated at room temperature in the dark for 45 min. The cells were then washed with PBS, stained for 5 min with antifade mounting medium with DAPI (300 μL $well^{-1}$) and observed by CLSM.

In vitro and in vivo MRI performance

For in vitro MRI tests, suspensions of La-BFO with different concentrations (0, 0.5, 1, 2, 4, 8 and 16 mg mL^{-1}) nanoparticles were prepared and systematically diluted. A certain concentration of diluted medium in a 96-well plate was placed vertically in the head tray at room temperature. MRI was performed using a clinical 3T whole-body MRI scanner (Canon 3.0T Vantage Titan). Transverse relaxation R2 was measured using a multi-echo spin-echo sequence in which TR was fixed at 2017 ms and TE at (16, 32, 48, 64) ms. In this sequence mode, the slice thickness (3 mm), the field of view (FOV, 150 * 160 mm), and matrix size (256 * 256 pixels) values were kept constant, and T_2-weighted MRI phantoms were produced for analysis. Signal intensity was then collected within the region of interest (ROI) at all T_2 values. For in vivo MRI tests, a typical tumor model was formed by injecting 4T1 cancer cells (100 μL) containing 1×10^6 4T1 cancer cells into the back of Balb/c mice. After approximately 2 weeks of rearing, tumors with a diameter of approximately 1 cm were observed on their backs. In vivo, experiments were performed using 4T1 hormonal mice anesthetized with 4% aldehyde hydrate and injected intravenously (i.v, via the tail vein) with 100 μL of La-BFO (10 mg mL^{-1}) solution. MRI detection was initiated immediately after injection. Anesthetized mice were placed in a rat coil at room temperature. The scanning mode and signal intensity at T_2 values were acquired.

In vitro and in vivo CT performance

For in vitro CT imaging, La-BFO nanoparticles were diluted at concentrations of 0, 0.5, 1, 2, 4, 8 and 16 mg mL^{-1}. In the body portion, anesthetized 4T1 hormonal mice were subjected to tail vein injection of 100 μL of La-BFO (10 mg mL^{-1}) solution. CT shadows were then prepared using a Siemens 128-row second-generation dual-source CT machine (Somatom Definition FLASH) CT scanner. The field of view (185 mm), image matrix (512 * 512), and slice thickness (1 mm) were fixed, and the X-ray voltage (120 kV) and anode current (98 mA) were set. CT signal intensity was determined for the region of interest (ROI) Hounsfield unit (HU) using Image J software.

In vivo imaging and biodistribution.

For in vivo imaging, BLAB/c nude mice were intravenously injected with Cy5.5-labelled La-BFO nanoparticles (10 mg mL^{-1}, 100 μl). Fluorescence imaging of mice was performed at different time points. La-BFO nanoparticles were intravenously injected into BLAB/c nude mice. The main organ samples were collected, weighed, and digested in aqua regia. The contents of Fe in each organ were determined by inductively coupled plasma mass spectrometry (ICP-MS).

Animal experiments

4-week-old Female Balb/c mice were purchased from Shanghai SLAC Laboratory Animal Co., Ltd. The animal experiment was conducted with the approval of ethics by the ethics committee of Shanghai University. The 4T1 breast cancer model was established through subcutaneously injecting of 1×10^6 4T1 cancer cells (100 μL). When tumor sizes were about ~ 100 mm^3, tumor-bearing Balb/c mice were randomly allocated into six groups ($n = 5$): (1) Control; (2) US (1.5 W cm^{-2}, 50% duty cycle, 5 min); (3) La-BFO *i.v.* (10 mg mL^{-1}, 100 μl); (4) La-BFO *i.t.* (10 mg mL^{-1}, 100 μl); (5) La-BFO *i.v.* (10 mg $mL^{-1,}$ 100 μl) + US (1.5 W cm^{-2}, 50% duty cycle, 5 min); (6) La-BFO *i.t.* (10 mg mL^{-1}, 100 μl) + US (1.5 W cm^{-2}, 50% duty cycle, 5 min). On days 1, 3, 5 and 7, the US irradiation operation was executed. The body weights and tumor sizes were measured every other day. The tumor volume was calculated using the following formula: tumor

volume = length × width^2/2. The mice were sacrificed after two weeks post-treatment and the tumors were collected. The tumor inhibition rates of each group were calculated using the following equation: tumor inhibition rates = (V_{14}, control - V_{14}, experiment)/V_{14}, control × 100%. Finally, tumors and major organs (heart, liver, spleen, lung, kidney) of different groups were collected and sectioned for H&E staining, Ki-67, TUNEL, cleaved Caspase-1 and N-GSDMD immunofluorescence staining.

Distant tumor Inhibition

3×10^6 4T1 cells were subcutaneously injected into the left hind limb of mice to construct the original tumor model, and 2×10^5 4T1 cells were injected into the right hind limb to establish the metastatic tumor model. When the tumor volume reached about 60 mm^3, the mice were randomly divided into 2 groups ($n = 4$): (1) control group, (2) La-BFO *i.v.* (10 mg mL^{-1}, 100 μl) + US (1.5 W cm^{-2}, 50% duty cycle, 5 min). After 12 days of treatment, the mice were sacrificed and the tumors were collected.

Statistical analysis

Statistical analysis was performed by one-way ANOVA. $^*p < 0.05$, $^{**}p < 0.01$, $^{***}p < 0.001$, and $^{****}p < 0.0001$.

Computational details

All the calculations are performed in the framework of the density functional theory with the projector-augmented plane-wave method, as implemented in the Vienna ab initio simulation package [39]. The generalized gradient approximation proposed by Perdew-Burke-Ernzerhof (PBE) is selected for the exchange-correlation potential [40]. The cut-off energy for the plane wave is set to 500 eV. The energy criterion is set to 10 – 5 eV in the iterative solution of the Kohn-Sham equation. All the structures are relaxed until the residual forces on the atoms have declined to less than 0.03 eV/A.

Supplementary Information

The online version contains supplementary material available at https://doi.org/10.1186/s12951-025-03411-0.

Supplementary Material 1

Acknowledgements
The schematic illustrations in the figures were created with BioRender.com.

Author contributions
X. Li: Writing-original draft, Visualization, Methodology, Investigation. Y. Wang: Writing-original draft, Methodology, Investigation. X. Cao: Writing-original draft, Methodology, Investigation. X. Song: Investigation, Methodology, Software. L. Chen: Investigation, Methodology, Software. M. Chang: Writing-review & editing, Writing-original draft, Visualization, Project administration. Y. Chen: Writing-review & editing, Writing-original draft, Visualization, Project administration, Methodology, Investigation, Formal analysis, Data curation, Conceptualization, Validation. B. Huang: Writing-review & editing, Visualization, Project administration, Methodology, Investigation.

Funding
This work was financially supported by the National Natural Science Foundation of China (Grant No. 82372029, 81400793), Discipline Construction of Pudong New Area Health Commission (Grant No. PWZxk2022-03), Shanghai Pudong New District Health Committee Health Industry Special Project (PW2024E-02), The Investigator-initiated Trial Program of Shanghai Pudong New Area Health Commission (the Cohort Study Program, 2025-PWDL-24).

Data availability
No datasets were generated or analysed during the current study.

Declarations

Ethics approval and consent to participate
The animal experiment was conducted with the approval of ethics by Ethic Committee of Shanghai University.

Consent for publication
All authors agreed to submit this manuscript.

Competing interests
The authors declare no competing interests.

Received: 9 January 2025 / Accepted: 19 April 2025
Published online: 03 May 2025

References

1. Kumagai S, Itahashi K, Nishikawa H. Regulatory T cell-mediated immunosuppression orchestrated by cancer: towards an immuno-genomic paradigm for precision medicine. Nat Rev Clin Oncol. 2024;21:337–53.
2. Sheikh A, Kesharwani P, Almalki WH, Almujri SS, Dai L, Chen Z-S, et al. Understanding the novel approach of nanoferroptosis for Cancer therapy. Nano-Micro Lett. 2024;16:188.
3. Yu P, Zhang X, Liu N, Tang L, Peng C, Chen X. Pyroptosis: mechanisms and diseases. Signal Transduct Target Ther. 2021;6:128.
4. Minton K. Pyroptosis heats tumour immunity. Nat Rev Immunol. 2020;20:274–75.
5. Chang M, Wang Z, Dong C, Zhou R, Chen L, Huang H, et al. Ultrasound-Amplified enzyodynamic tumor therapy by perovskite Nanoenzyme-Enabled cell pyroptosis and cascade catalysis. Adv Mater. 2023;35:2208817.
6. Deng W, Bai Y, Deng F, Pan Y, Mei S, Zheng Z, et al. Streptococcal pyrogenic exotoxin B cleaves GSDMA and triggers pyroptosis. Nature. 2022;602:496–502.
7. Ma X, Hao J, Wu J, Li Y, Cai X, Zheng Y. Prussian blue nanozyme as a pyroptosis inhibitor alleviates neurodegeneration. Adv Mater. 2022;34:2106723.
8. Xu K, Chang M, Wang Z, Yang H, Jia Y, Xu W, et al. Multienzyme-Mimicking $LaCoO_3$ nanotrigger for programming Cancer-Cell pyroptosis. Adv Mater. 2023;35:2302961.
9. Liang CY, Chang KF, Huang YC, Huang XF, Sheu GT, Kuo CF, et al. Patchouli alcohol induces G_0/G_1 cell cycle arrest and apoptosis in vincristine-resistant non-small cell lung cancer through ROS-mediated DNA damage. Thorac Cancer. 2023;14:2007–17.
10. Kim H, Yoon J, Kim HK, Lee WT, Nguyen NT, Le XT, et al. Upconverting nanoparticle-containing erythrocyte-sized hemoglobin microgels that generate heat, oxygen and reactive oxygen species for suppressing hypoxic tumors. Bioact Mater. 2023;22:112–26.
11. Wang Z, Ren X, Li Y, Qiu L, Wang D, Liu A, et al. Reactive oxygen species amplifier for Apoptosis-Ferroptosis mediated High-Efficiency radiosensitization of tumors. ACS Nano. 2024;18:10288–301.
12. Du G, Healy LB, David L, Walker C, El-Baba TJ, Lutomski CA, et al. ROS-dependent S-palmitoylation activates cleaved and intact gasdermin D. Nature. 2024;630:437–46.
13. Yu L, Xu Y, Pu Z, Kang H, Li M, Sessler JL, et al. Photocatalytic superoxide radical generator that induces pyroptosis in Cancer cells. J Am Chem Soc. 2022;144:11326–37.
14. Li J, Liu X, Zheng Y, Cui Z, Jiang H, Li Z, et al. Achieving fast charge separation by ferroelectric ultrasonic interfacial engineering for rapid sonotherapy of Bacteria-Infected osteomyelitis. Adv Mater. 2023;35:2210296.

15. Tian B, Tian R, Liu S, Wang Y, Gai S, Xie Y, et al. Doping engineering to modulate lattice and electronic structure for enhanced piezocatalytic therapy and ferroptosis. Adv Mater. 2023;35:2304262.
16. Deng R, Zhou H, Qin Q, Ding L, Song X, Chang M, et al. Palladium-Catalyzed hydrogenation of black barium titanate for Multienzyme-Piezoelectric synergetic tumor therapy. Adv Mater. 2024;36:2307568.
17. Wang Q, Tian Y, Yao M, Fu J, Wang L, Zhu Y. Bimetallic organic frameworks of high piezovoltage for Sono-Piezo dynamic therapy. Adv Mater. 2023;35:2301784.
18. Huang Y, Wan X, Su Q, Zhao C, Cao J, Yue Y, et al. Ultrasound-activated piezohot carriers trigger tandem catalysis coordinating cuproptosis-like bacterial death against implant infections. Nat Commun. 2024;15:1643.
19. Paull O, Xu C, Cheng X, Zhang Y, Xu B, Kelley KP, et al. Anisotropic epitaxial stabilization of a low-symmetry ferroelectric with enhanced electromechanical response. Nat Mater. 2022;21:74–80.
20. Chen X, Sun D, He Z, Kang S, Miao Y, Li Y. Ferrite bismuth-based nanomaterials: from ferroelectric and piezoelectric properties to nanomedicine applications. Colloid Surf B. 2024;233:113642.
21. Yonesato K, Yanai D, Yamazoe S, Yokogawa D, Kikuchi T, Yamaguchi K, et al. Surface-exposed silver nanoclusters inside molecular metal oxide cavities. Nat Chem. 2023;15:940–47.
22. Du X, Huang J, Zhang J, Yan Y, Wu C, Hu Y, et al. Modulating electronic structures of inorganic nanomaterials for efficient electrocatalytic water splitting. Angew Chem Int Ed. 2019;58:4484–502.
23. Lan S, Yu C, Sun F, Chen Y, Chen D, Mai W, et al. Tuning piezoelectric driven photocatalysis by La-doped magnetic $BiFeO_3$-based multiferroics for water purification. Nano Energy. 2022;93:106792.
24. Mirshafiee V, Sun B, Chang CH, Liao Y-P, Jiang W, Jiang J, et al. Toxicological profiling of metal oxide nanoparticles in liver context reveals pyroptosis in Kupffer cells and macrophages versus apoptosis in hepatocytes. ACS Nano. 2018;12:3836–52.
25. Sun B, Han P, Zhao W, Liu Y, Chen P. White-Light-Controlled magnetic and ferroelectric properties in multiferroic $BiFeO_3$ square nanosheets. J Phys Chem C. 2014;118:18814–19.
26. Park T-J, Papaefthymiou GC, Viescas AJ, Moodenbaugh AR, Wong SS. Size-Dependent magnetic properties of Single-Crystalline multiferroic $BiFeO_3$ nanoparticles. Nano Lett. 2007;7:766–72.
27. Sankar Ganesh R, Sharma SK, Sankar S, Divyapriya B, Durgadevi E, Raji P, et al. Microstructure, structural, optical and piezoelectric properties of $BiFeO_3$ nanopowder synthesized from sol-gel. Curr Appl Phys. 2017;17:409–16.
28. Yin J, Liao G, Zhou J, Huang C, Ling Y, Lu P, et al. High performance of magnetic $BiFeO_3$ nanoparticle-mediated photocatalytic ozonation for wastewater decontamination. Sep Purif Technol. 2016;168:134–40.
29. Wang J, Neaton JB, Zheng H, Nagarajan V, Ogale SB, Liu B, et al. Epitaxial $BiFeO_3$ multiferroic thin film heterostructures. Science. 2003;299:1719–22.
30. Bogdan J, Pławińska-Czarnak J, Zarzyńska J. Nanoparticles of titanium and zinc oxides as novel agents in tumor treatment: a review. Nanoscale Res Lett. 2017;12:225.
31. Desideri E, Ciccarone F, Ciriolo MR. Targeting glutathione metabolism: partner in crime in anticancer therapy. Nutrients. 2019;11:1926.
32. Lin B, Chen H, Liang D, Lin W, Qi X, Liu H, et al. Acidic pH and High-H_2O_2 dual tumor Microenvironment-Responsive nanocatalytic graphene oxide for Cancer selective therapy and recognition. ACS Appl Mater Interfaces. 2019;11:11157–66.
33. Lan S, Chen Y, Zeng L, Ji H, Liu W, Zhu M. Piezo-activation of peroxymonosulfate for benzothiazole removal in water. J Hazard Mater. 2020;393:122448.
34. Zhou X, Yan F, Wu S, Shen B, Zeng H, Zhai J. Remarkable piezophoto coupling catalysis behavior of BiOX/$BaTiO_3$ (X = Cl, Br, Cl0.166Br0.834) piezoelectric composites. Small. 2020;16:2001573.
35. Temeeprasertkij P, Iwaoka M, Iwamori S. Theoretical investigation on the selective hydroxyl Radical–Induced decolorization of Methylene-Blue-Dyed polymer films. Comput. 2022;10:169.
36. Zheng Z, Deng W, Bai Y, Miao R, Mei S, Zhang Z, et al. The lysosomal Rag-Ragulator complex licenses RIPK1– and caspase-8–mediated pyroptosis by Yersinia. Science. 2021;372:eabg0269.
37. Lusic H, Grinstaff MW. X-ray-Computed tomography contrast agents. Chem Rev. 2013;113:1641–66.
38. Dash A, Blasiak B, Tomanek B, Banerjee A, Trudel S, Latta P, et al. Colloidally stable monodisperse Fe nanoparticles as T_2 contrast agents for High-Field clinical and preclinical magnetic resonance imaging. ACS Appl Nano Mater. 2021;4:1235–42.
39. Kresse G, Joubert D. From ultrasoft pseudopotentials to the projector augmented-wave method. Phys Rev B. 1999;59:1758–75.
40. Perdew JP, Burke K, Ernzerhof M. Generalized gradient approximation made simple. Phys Rev Lett. 1996;77:3865–68.

Publisher's note